

Biomimetic Macrophage Membrane-Camouflaged Nanoparticles Induce Ferroptosis by Promoting Mitochondrial Damage in Glioblastoma

Zhengcong Cao,[#] Xiao Liu,[#] Wangqian Zhang,[#] Keying Zhang,[#] Luxiang Pan, Maorong Zhu, Haozhe Qin, Cheng Zou, Weizhong Wang, Cong Zhang, Yalong He, Wei Lin, Yingqi Zhang, Donghui Han,^{*} Meng Li,^{*} and Jintao Gu^{*}



Cite This: *ACS Nano* 2023, 17, 23746–23760



Read Online

ACCESS |

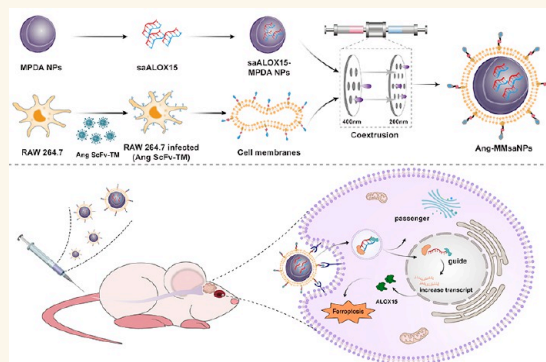
Metrics & More

Article Recommendations

Supporting Information

ABSTRACT: The increasing understanding of ferroptosis has indicated its role and therapeutic potential in cancer; however, this knowledge has yet to be translated into effective therapies. Glioblastoma (GBM) patients face a bleak prognosis and encounter challenges due to the limited treatment options available. In this study, we conducted a genome-wide CRISPR–Cas9 screening in the presence of a ferroptosis inducer (RSL3) to identify the key driver genes involved in ferroptosis. We identified ALOX15, a key lipoxygenase (LOX), as an essential driver of ferroptosis. Small activating RNA (saRNA) was used to mediate the expression of ALOX15 promoted ferroptosis in GBM cells. We then coated saALOX15-loaded mesoporous polydopamine (MPDA) with Angiopep-2-modified macrophage membranes (MMs) to reduce the clearance by the mononuclear phagocyte system (MPS) and increase the ability of the complex to cross the blood–brain barrier (BBB) during specific targeted therapy of orthotopic GBM. These generated hybrid nanoparticles (NPs) induced ferroptosis by mediating mitochondrial dysfunction and rendering mitochondrial morphology abnormal. In vivo, the modified MM enabled the NPs to target GBM cells, exert a marked inhibitory effect on GBM progression, and promote GBM radiosensitivity. Our results reveal ALOX15 to be a promising therapeutic target in GBM and suggest a biomimetic strategy that depends on the biological properties of MMs to enhance the in vivo performance of NPs for treating GBM.

KEYWORDS: glioblastoma, ferroptosis, macrophage membrane, nanoparticle, ALOX15

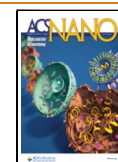


INTRODUCTION

Glioblastoma (GBM) is the most common malignant tumor of the central nervous system (CNS), which is characterized by rapid growth, dissemination through the normal brain, and resistance to treatment, resulting in poor prognosis.¹ Current treatment options are limited to maximal surgical resection followed by radiotherapy (RT) and adjuvant chemotherapy.² The main obstacle to treating GBM is the blood–brain barrier (BBB), which is composed mainly of endothelial cells, pericytes, astrocytes, and microglial cells and functions as a critical protector of the CNS microenvironment by preventing waste in the blood from entering the CNS and thereby maintaining CNS homeostasis.³ It is difficult for large-molecule drugs to penetrate the BBB and enter the CNS; moreover, even drugs that can enter the CNS must overcome the action of efflux pumps such as P-

glycoprotein in the luminal membrane, which exports drugs out of the CNS to impede GBM treatment drug accumulation and reduce their efficacy.^{4,5} To treat GBM, a higher drug dosage is usually required and high dosing may lead to many severe side effects. Therefore, it is crucial to investigate methods for enabling drug penetration through the BBB and identifying

Received: August 12, 2023
Revised: November 16, 2023
Accepted: November 17, 2023
Published: November 22, 2023



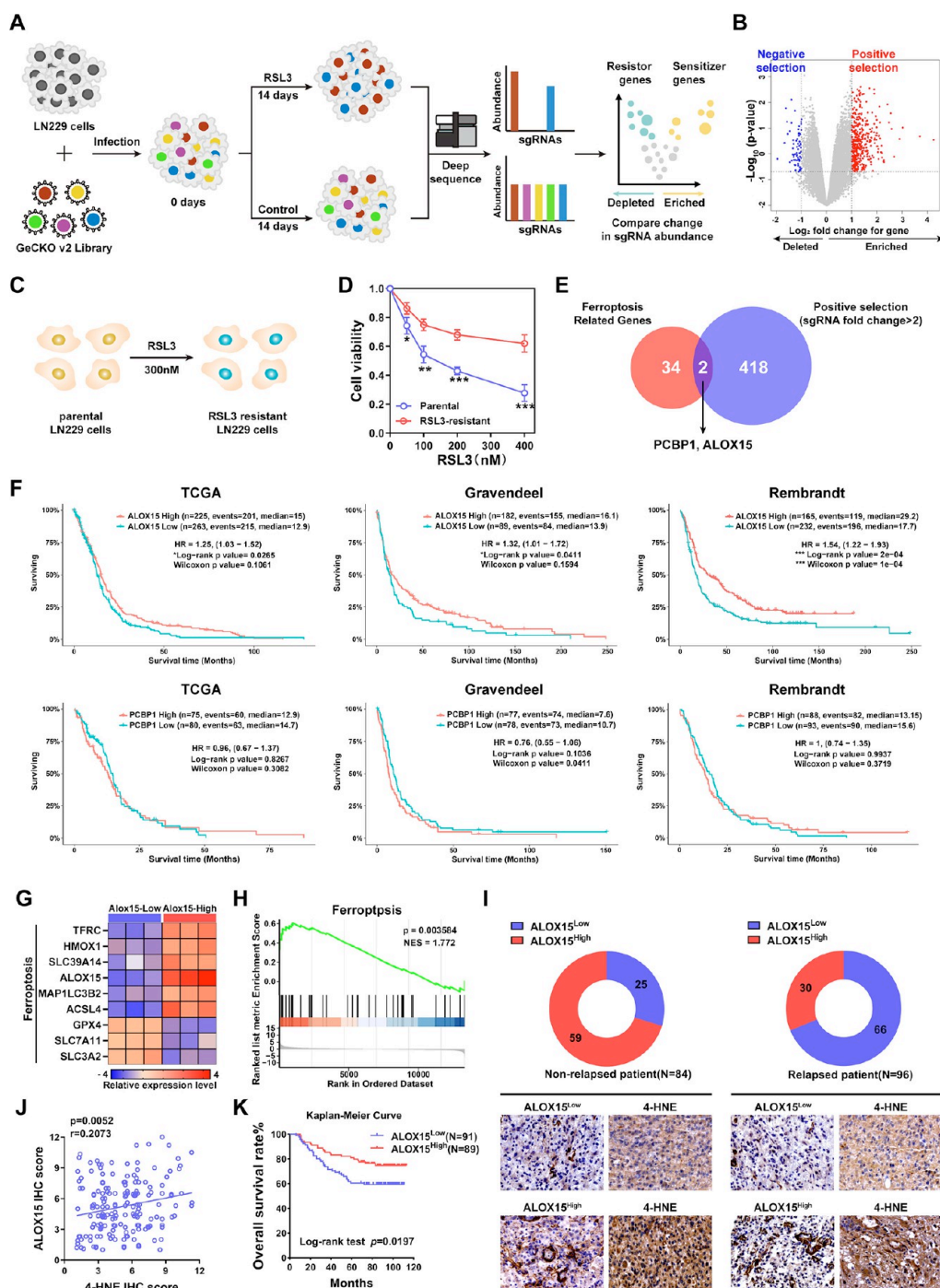


Figure 1. Genome-wide CRISPR–Cas9 library screening and RNA sequencing led to the identification of ALOX15 as an essential driver of ferroptosis in glioma. (A) Schematics of the experimental design. (B) Volcano plot displaying the log₂ fold change and adjusted *P* value for all sgRNAs identified in the screen. (C) Induction of RSL3-resistant cells from parental LN229 cells by RSL3 treatment. RNA-Seq was performed in RSL3-resistant cells in parallel with parental cells. (D) RSL3-resistant LN229 cells and parental LN229 cells were treated with RSL3 with the gradient concentrations. IC₅₀ was assessed by cell counting kit-8 (CCK-8) at 48 h. (E) Venn diagrams show overlapped essential driver genes for ferroptosis. (F) Prognostic significance of ALOX15 and PCBP1 up-regulation in glioma in TCGA, Gravendeel and Rembrandt databases. (G) RNA-seq was performed in patients with high ALOX15 expression and low ALOX15 expression. (H) GSEA demonstrated that ferroptosis-related genes were significantly enriched following glioma samples with high expression of ALOX15. (I) Representative images of IHC staining of ALOX15 in specimens of nonrelapsed and relapsed patients. (J) Pearson correlation analysis revealed that the expression of ALOX15 was positively correlated with the expression of 4-HNE. (K) Kaplan–Meier estimate of survival time for glioma patients with low versus high expression of ALOX15.

specific therapeutic targets for the diagnosis and treatment of GBM.

Ferroptosis is a complex and highly regulated process involving the dysregulation of iron homeostasis, glutathione

metabolism, and lipid peroxidation.⁶ Several studies have demonstrated the important role of ferroptosis in various tumors, including lung cancer, ovarian cancer, leukemia, and glioma.^{7,8} Furthermore, the selective induction of ferroptosis has

been used as a potential therapeutic strategy for certain cancers. However, ferroptosis activation involves a series of complexes that reciprocally regulate redox homeostasis, lipid metabolism, and iron metabolism, which are physiological processes equally important for maintaining normal cell homeostasis and physiological functions.⁹ For example, ferroptosis induction by a GPX4 inhibitor leads to a decline in the development and function of the nervous system and kidney because the GPX4 gene is fundamental to embryonic development and homeostasis in some adult mouse tissues.¹⁰ Therefore, when ferroptosis inducers are administered intravenously, they indiscriminately attack cells throughout the body, possibly causing severe toxic side effects that limit the specificity and clinical application of these drugs. The identification of key targets of ferroptosis in tumor cells shows the potential to advance the use of ferroptosis-promoting drugs for tumor therapy.

Several genome-wide high-throughput screening methods have been applied to unbiasedly identify key genes associated with drug resistance in human cancers. Previously, RNA interference (RNAi) screening with a short interfering RNA (shRNA) library was performed to identify target genes to knock down.¹¹ However, inefficient gene knockdown and off-target effects limit their potential applications. Recently, the innovative CRISPR-Cas9 library system with genome editing technology provides another opportunity to overcome these limitations.¹² CRISPR/Cas9 library screening has been used to identify genes associated with cancer cell survival, migration, and resistance to therapeutic drug treatment in various models. However, CRISPR screens to identify key genes involved in ferroptosis have not been reported.

Recently, increasing attention has been paid to biomimetic drug delivery systems, especially cell membrane-coated nanoparticles (NPs).¹³ Nanoparticles camouflaged by biological cell membranes have recently been the focus of attention for their prolonged circulation in vivo.¹⁴ Its intrinsic self-recognition properties optimize its dynamic properties by masking its contents to avoid clearance by the mononuclear phagocyte system (MPS) and immune surveillance.¹⁵ Membrane camouflage strategies can extend the half-life of nanoparticles in systemic circulation and increase tumor adhesion without losing their drug-loading capacity or nanosize advantages.¹⁶ Various delivery vehicles, such as gold-based nanoplateforms, upconversion nanoparticles, and mesoporous silica nanoparticles, have been used in macrophage membrane (MM) systems and exhibit high stability in systemic circulation.¹⁷ The intrinsic chemotactic capacity of inflammation-induced macrophages may promote the accumulation of vectors in chronic inflammatory tumor tissue. However, barriers to targeted medicine delivery by MM-camouflaged systems remain.

In this study, we performed genome-wide screening using a CRISPR-Cas9 genome editing system in GBM cells to explore the genes critical for ferroptosis. We identified ALOX15, a key lipoxygenase (LOX) in the ferroptosis pathway that promotes peroxidation of polyunsaturated fatty acids (PUFAs), as a driver gene of GBM cell ferroptosis. Furthermore, we developed Angiopep-2-modified MM-coated biomimetic NPs for use in the targeted therapy of GBM. We first encapsulated the small activating RNA (saRNA) of ALOX15 in mesoporous polydopamine (MPDA) and then coated the saALOX15-loaded MPDA with a modified MM, thereby creating Ang-MMsaNPs for use in the targeted and efficient management of GBM. Mechanistically, we found that Ang-MMsaNPs led to abnormalities in mitochondrial function and a ferroptotic mitochondrial

morphology. The biodistribution, pharmacodynamics, and general tissue toxicity suggest that the Ang-MMsaNPs offer promise for use in GBM therapy.

RESULTS

CRISPR-Cas9-Based Screening Identifies ALOX15 as an Essential Driver for Ferroptosis in Glioma. In order to identify the critical driver genes involved in ferroptosis, we used a combination strategy based on a genome-wide screening of the CRISPR-Cas9 knockout library and the transcriptome analysis of RSL3-resistant cell lines (Figure 1A). The asymmetric nature of the volcano plot revealed that the statistical power to detect depleted sgRNAs was lower than the power to detect enriched sgRNAs (Figure 1B). Therefore, using this strategy, we identified a series of sgRNAs targeting 418 genes that were significantly enriched in RSL3-treated cells compared to dimethyl sulfoxide (DMSO)-treated cells.

Parallel to CRISPR-Cas9 knockout library screening, we performed RNA-seq to monitor the transcriptome changes in LN229 cells after RSL3 treatment that was applied for as long as 3 months (Figure 1C). Successful development of RSL3-resistant cells was demonstrated by increased cell viability and reduced ferroptosis rates during the RSL3 treatment (Figure 1D). RNA-seq identified 34 genes associated with ferroptosis among the differentially expressed genes (Supplementary Figure S1). Differentially expressed genes associated with ferroptosis and identified in the transcriptome analysis were then compared with CRISPR-Cas9-knockout screened genes. Based on the comparison, two genes (ALOX15 and PCBP1) overlapped in the two data sets and were associated with ferroptosis in GBM (Figure 1E). We validated the two genes in the databases of TCGA, Gravendeel, and Rembrandt. Notably, ALOX15 levels were significantly correlated with poor prognosis, according to the three public databases, while PCBP1 exerted no effect on prognosis (Figure 1F). We therefore chose ALOX15, a key lipoxygenase (LOX) in the ferroptosis pathway that promotes the peroxidation of PUFAs, for further functional analysis. Six glioma samples were chosen for RNA-seq analysis based on their ALOX15 expression levels. Specifically, three samples exhibited high ALOX15 expression, while the other three samples exhibited low ALOX15 expression (Figure 1G). A gene set enrichment analysis (GSEA) revealed the activation of ferroptosis in glioma samples with high levels of ALOX15 (Figure 1H). Consistently, the expression of ALOX15 was closely linked with the ACSL4 level in the Gravendeel, Rembrandt, TCGA, and CGGA databases (Supplementary Figure S2). To further investigate the clinical relationship between ALOX15 expression and poor prognosis in glioma patients, we obtained a tissue microarray of 180 glioma tumor samples and stained them with anti-ALOX15 and anti-4-HNE (a marker of cells undergoing ferroptosis) antibodies. Interestingly, decreased ALOX15 levels were observed in glioma patients who experienced relapse. When dividing the patients into high and low ALOX15 expression groups, using the median expression value as the threshold, we observed a significant decrease in the percentage of patients exhibiting low ALOX15 expression in the nonrelapsed patient group compared to the relapsed patient group, which revealed that patients in “ALOX15-low” glioma group were more prone to disease relapse (Figure 1I). Pearson correlation analysis showed that the ALOX15 expression was positively correlated with 4-HNE expression (Figure 1J). Kaplan-Meier survival analysis showed that lower ALOX15 levels in glioma patients are associated with reduced overall

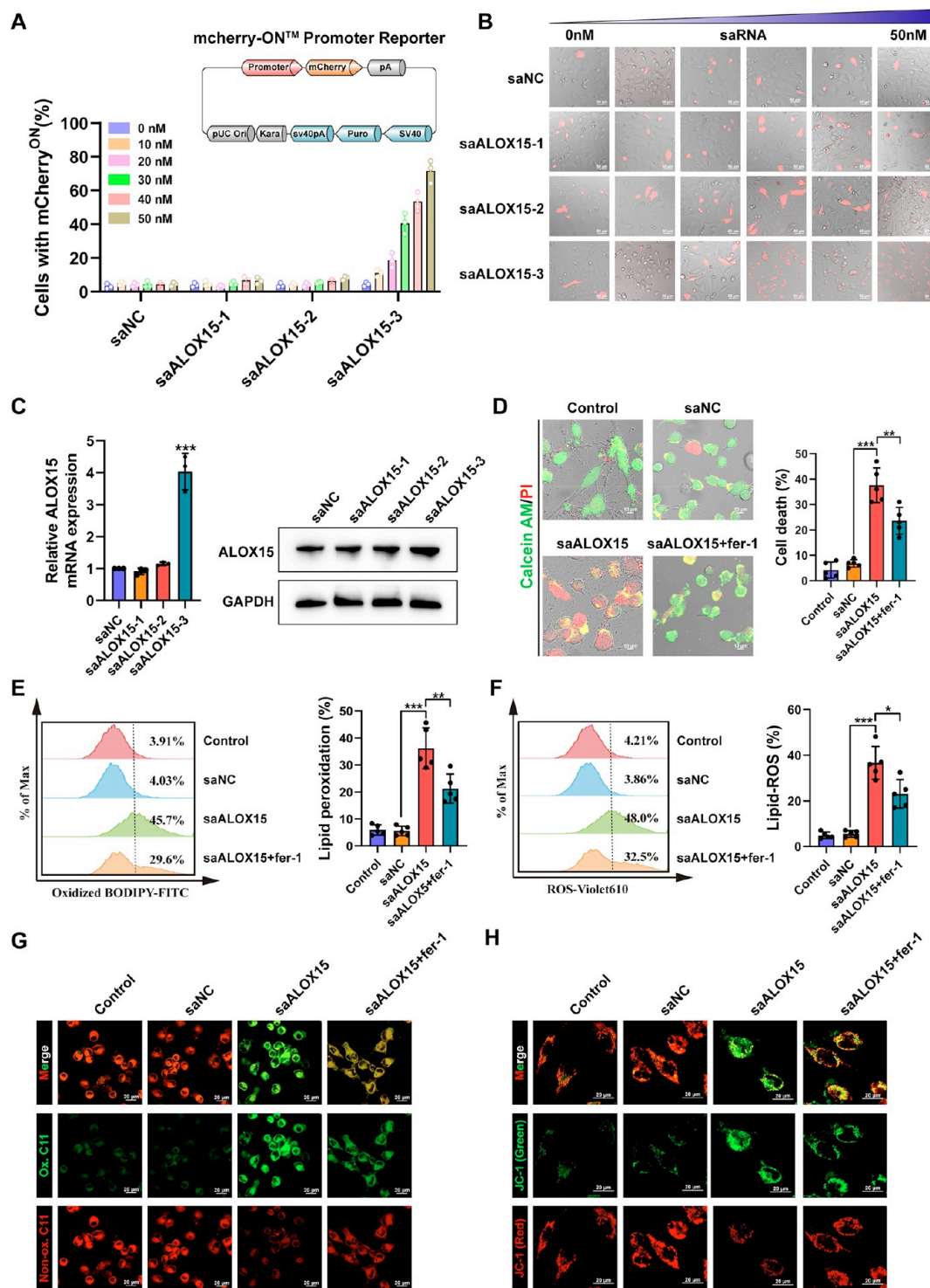


Figure 2. SaALOX15-mediated activation of ALOX15 promotes ferroptosis in GBM cells. (A, B) A fluorescent reporter system was constructed to indicate the activation of the ALOX15 promoter. LN229 cells were transfected with saALOX15 with the gradient concentrations, and the level of mcherry-ON was measured by a confocal microscope. Scale bar = 10 μ m. (C) qRT-PCR and immunoblot were used to detect the overexpress efficiency of saALOX15. (D) Detection of living and dead cells. Scale bar = 10 μ m. (E) The ratio of oxidized to nonoxidized lipids. (F) Liperflu staining visualized lipid ROS in cells after treatment. (G) Confocal microscopy visualized the alterations in lipid peroxidation in LN229 cells after C11-BODIPY probe staining. Scale bar = 10 μ m. (H) Confocal microscopy visualized the alterations in MMP ($\Delta\psi$ m) in LN229 cells after JC-1 staining. Scale bar = 10 μ m.

survival (Figure 1K). These findings further highlight that ALOX15 is a critical determinant of ferroptosis in glioma.

Small Activating RNA-Mediated Activation of ALOX15 Promotes Ferroptosis in GBM Cells. Small activating RNA

(saRNA) functions by recruiting endogenous transcription complexes to target genes, leading to increased expression of mRNAs and upregulation of target proteins.¹⁸ saRNAs have been effectively utilized in RNA activation (RNAa) to stimulate

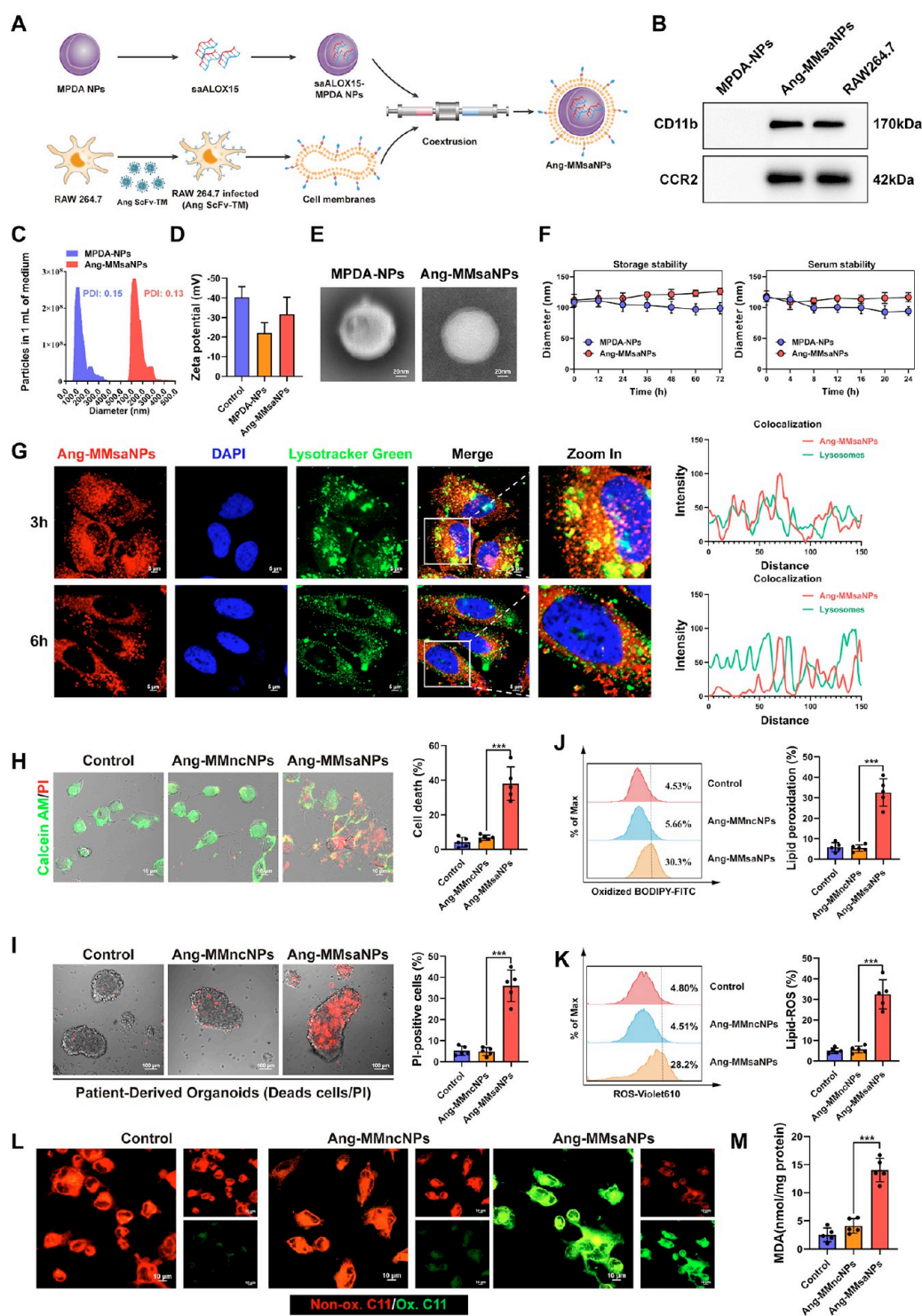


Figure 3. Synthesis and characterization of Ang-MMsaNPs. (A) Construction schematic diagram of Ang-MMsaNPs. (B) Biomarkers of macrophage membrane (MM) detected by Immunoblot. (C) Hydrodynamic diameter change analysis of NPs. (D) Zeta potential change analysis of NPs. (E) Transmission electron microscopy images of purified NPs. (F) Detection of the stability of NPs. (G) In vitro endosomal escape capability of Ang-MMsaNPs in LN229 cells by confocal microscopy. Scale bar = 5 μm . (H) Detection of living and dead cells after Ang-MMsaNPs treatment. Scale bar = 10 μm . (I) Detection of living and dead cells in PDOs after Ang-MMsaNPs treatment. Scale bar = 100 μm . (J) The ratio of oxidized to nonoxidized lipids after Ang-MMsaNPs treatment. (K) Liperfluor staining visualized lipid ROS in cells after Ang-MMsaNPs treatment. (L) Confocal microscopy visualized the alterations in lipid peroxidation after Ang-MMsaNPs treatment. Scale bar = 10 μm . (M) The expression level of lipid peroxidation products (MDA) after Ang-MMsaNPs treatment.

gene expression in cultured cells, and thereby, we reasoned that this emerging technique could allow us to develop various biotechnological applications without synthesizing dangerous constructs containing an exogenous DNA sequence. Therefore,

we designed three saRNAs to activate ALOX15 (Supplementary Table S1). A fluorescent reporter system was constructed to investigate the activation of the ALOX15 promoter based on the working principle of the saRNAs. Then, saALOX15-3 was found

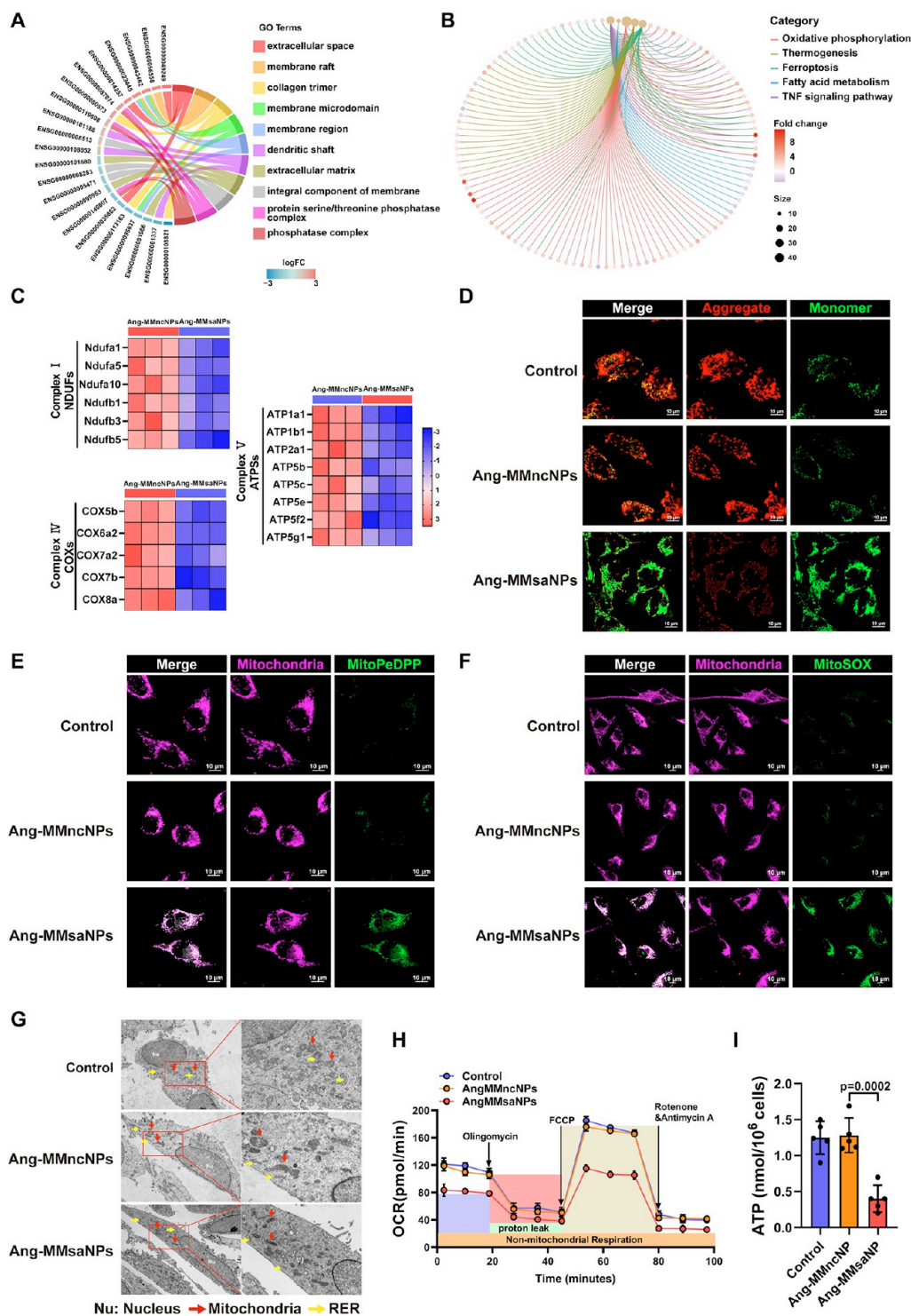


Figure 4. Ang-MMsNPs induce GBM ferroptosis by promoting mitochondrial damage. (A) The Gene Ontology (GO) function enrichment analysis. (B) KEGG enrichment analysis of genes differentially expressed after Ang-MMsNPs treatment. (C) Differential expression analysis of the mitochondrial electron transport chain (ETC) complexes I (NDUFS), IV (COXS), and V (ATPSs) related genes after Ang-MMsNPs treatment. (D) Confocal microscopy visualized the alterations in MMP ($\Delta\psi_m$) after Ang-MMsNPs treatment. Scale bar = 10 μm . (E) Confocal microscopy visualized the alterations in mitochondrial lipid peroxidation after MitoPeDPP and MitoBright LT Deep Red staining. Scale bar = 10 μm . (F) Confocal microscopy visualized the alterations in mitochondrial ROS after MitoSOX and MitoBright LT Deep Red staining. Scale bar = 10 μm . (G) Transmission electron microscopy images of LN229 cells after Ang-MMsNPs treatment. Nu, nucleus; red arrows, mitochondria; yellow arrows, rough endoplasmic reticulum. (H) The real-time oxygen consumption rate (OCR) was measured after Ang-MMsNPs treatment by Seahorse XF extracellular flux analyzer. (I) The level of ATP after Ang-MMsNPs treatment.

to significantly enhance the activation of the mCherry reporter, while saALOX15-1 and saALOX15-2 did not exert this effect (Figure 2A,B). qRT-PCR and immunoblotting also proved that

saALOX15-3 upregulated ALOX15 to the highest degree (Figure 2C and Supplementary Figure S3). We further investigated whether saALOX15-3 aggravates ferroptosis in

GBM cells. Ferroptotic cell death was observed when GBM cells were exposed to saALOX15 (representing saALOX15-3), and this effect was attenuated by ferroptosis-specific inhibitor ferrostatin-1 (Figure 2D). saALOX15 treatment significantly increased the proportion of oxidized lipids compared with total lipids (Figure 2E). Liperflu staining was used to visualize lipid reactive oxygen species (ROS), the levels of which were increased after the saALOX15 treatment (Figure 2F). C11-BODIPY probe staining revealed a significant increase in the ratio of oxidized to nonoxidized lipids following saALOX15 treatment, as determined by two-channel fluorescence analysis (Figure 2G). JC-1 staining indicated that the mitochondrial membrane potential (MMP, $\Delta\psi_m$) was significantly attenuated after saALOX15 treatment, as evidenced by an increased ratio of green-to-red fluorescence (Figure 2H). Taken together, these data support the conclusion that saALOX15 mediates the activation of ALOX15 to promote ferroptosis to levels sufficient to treat GBM cells.

Synthesis and Characterization of Ang-MMsANPs. Ang-MMsANPs were constructed using the following three-step process: (i) preparation of the saALOX15-loaded MPDA NPs, (ii) isolation of the Angiopep-2-modified MM, and (iii) covering of the MPDA-saANPs with the Angiopep-2-modified MM (Figure 3A and Supplementary Figure S4). Immunoblot analysis showed that the typical signals of CD11b and chemokine (C–C motif) receptor 2 (CCR2) in the MM were clearly observed in the Ang-MMsANPs and RAW264.7 cells but not in the MPDA-NPs (Figure 3B). The protein composition in MMs was more strongly retained in Ang-MMsANPs, but no protein signal was detected from MPDA-NPs, suggesting the successful translocation and retention of natural macrophage cell membranes onto the Ang-MMsANPs surface (Supplementary Figure S5). Compared to that of the uncoated MPDA-NPs, the hydrodynamic diameter of the Ang-MMsANPs increased from 104.63 to 115.25 nm, which has been attributed to the MM, which had a thickness of approximately 8 nm (Figure 3C). Furthermore, the zeta potential of the Ang-MMsANPs (−35.5 mV) was comparable to that of the original MM (−39.6 mV) but much higher than that of the unmodified MPDA-NPs (−22.7 mV) (Figure 3D). The transmission electron microscopy (TEM) image confirmed that Ang-MMsANPs showed a uniform “core–shell” morphology (Figure 3E). After long-term storage at room temperature, the Ang-MMsANPs remained at a relatively constant size and polydispersity index (PDI), indicating satisfactory stability (Figure 3F and Supplementary Figure S6). The encapsulation efficiency of the saRNA was similarly high in MPDA-NPs and Ang-MMsANPs (Supplementary Figure S7A). Ang-MMsANPs demonstrated a sustained release effect, possibly due to the formation of a physical barrier by the macrophage membrane wrapper, which delayed the release of saRNA (Supplementary Figure S7B). Collectively, these data suggest not only the successful envelopment of MPDA-NPs with MMs to form Ang-MMsANPs but also the preservation of the MM composition and retention of the tumor-tropism features to facilitate their intratumoral delivery. The escape of the NP content during endosomal confinement is a requirement for NP functionality, and we examined the *in vitro* endosomal escape capability of Ang-MMsANPs in LN229 cells via confocal microscopy. The Ang-MMsANPs showed high colocalization with lysosomes after a 3 h incubation. Interestingly, after 6 h of incubation, most of the Ang-MMsANPs and lysosomes did not overlap, suggesting that Ang-MMsANPs escaped from lysosomes over time (Figure 3G).

Subsequently, we evaluated the therapeutic efficacy of Ang-MMsANPs in LN229 cells. The ferroptosis-promoting effect of Ang-MMsANPs was determined by calcein-AM and propidium iodide (PI) staining, and in contrast to the other groups, the Ang-MMsANPs group emitted mostly red signals and few green signals (Figure 3H). The PI-positive (PI+) population also increased following Ang-MMsANPs treatment in patient-derived GBM organoids (PDOs) (Figure 3I). Similarly, the Ang-MMsANPs promoted ferroptotic functions, including massive lipid peroxidation, malondialdehyde (MDA), and lipid ROS accumulation (Figure 3J–M). Collectively, this evidence suggests the successful construction of Ang-MMsANPs and their therapeutic effect *in vitro*.

Ang-MMsANP-Induced Ferroptosis Is Caused by Mitochondrial Damage. To investigate how Ang-MMsANPs cause GBM cell ferroptosis, a global transcriptome analysis was performed. The Gene Ontology (GO) function enrichment analysis results indicated significant enrichment in membrane rafts, the membrane microdomain, the membrane region, and integral components of the membrane (Figure 4A). These GO results indicate that Ang-MMsANPs damage the cell membrane, which is also the main mechanism underlying ferroptosis. In addition, differentially expressed genes were mainly enriched in the KEGG categories of “thermogenesis”, “ferroptosis”, “lipid metabolism”, and “oxidative phosphorylation” (Figure 4B). Interestingly, a large fraction of downregulated differentially expressed genes encoded mitochondrial electron transport chain (ETC) complexes I (NDUFS), IV (COXs), and V (ATPSs), suggesting mitochondrial dysfunction after Ang-MMsANPs treatment (Figure 4C). The downregulation of these genes after treatment with Ang-MMsANPs was confirmed at the transcriptional level using qRT-PCR. (Supplementary Figure S8).

We further investigated whether Ang-MMsANPs cause mitochondrial dysfunction. Our research shows that the Ang-MMsANP-treated group had higher levels of JC-1 monomers than the control group, and this effect was accompanied by reduced $\Delta\psi_m$ (Figure 4D). The levels of mitochondrial lipid peroxidation in Ang-MMsANP-treated and untreated groups were assessed by MitoPeDPP, which is specifically oxidized by lipophilic peroxides in mitochondria. The Ang-MMsANPs group showed increased mitochondrial lipid peroxidation rates compared to those in the control cells (Figure 4E). To assess the levels of mitochondrial ROS, we captured images of cells treated with a MitoSOX Red fluorescent probe. This probe is highly sensitive to mitochondrial superoxide radicals and enables measurement of increases in mitochondrial ROS levels within cells. By analysis of the MitoSOX Green fluorescence of each sample, it was found that only $5.97 \pm 0.15\%$ of the cells in the control sample had high levels of mitochondrial ROS (mtROS). Treatment of LN229 cells with Ang-MMsANPs for 24 h resulted in a highly substantial increase in mtROS levels (the increase in cells with high MitoSOX Green fluorescence was $67.43 \pm 5.23\%$) (Figure 4F). These results are consistent with the abnormal mitochondrial function in ferroptotic cells.

In addition to mitochondrial dysfunction, an abnormal mitochondrial morphology is also an essential marker of ferroptosis. Electron microscopy observed severe deformation of mitochondria, and those in the Ang-MMsANP-treated group presented with fewer mitochondrial ridges, which are characteristic of ferroptosis (Figure 4G). The reactions associated with oxidative phosphorylation (OXPHOS) generate the MMP and drive the majority of ATP production in respiring cells. The real-

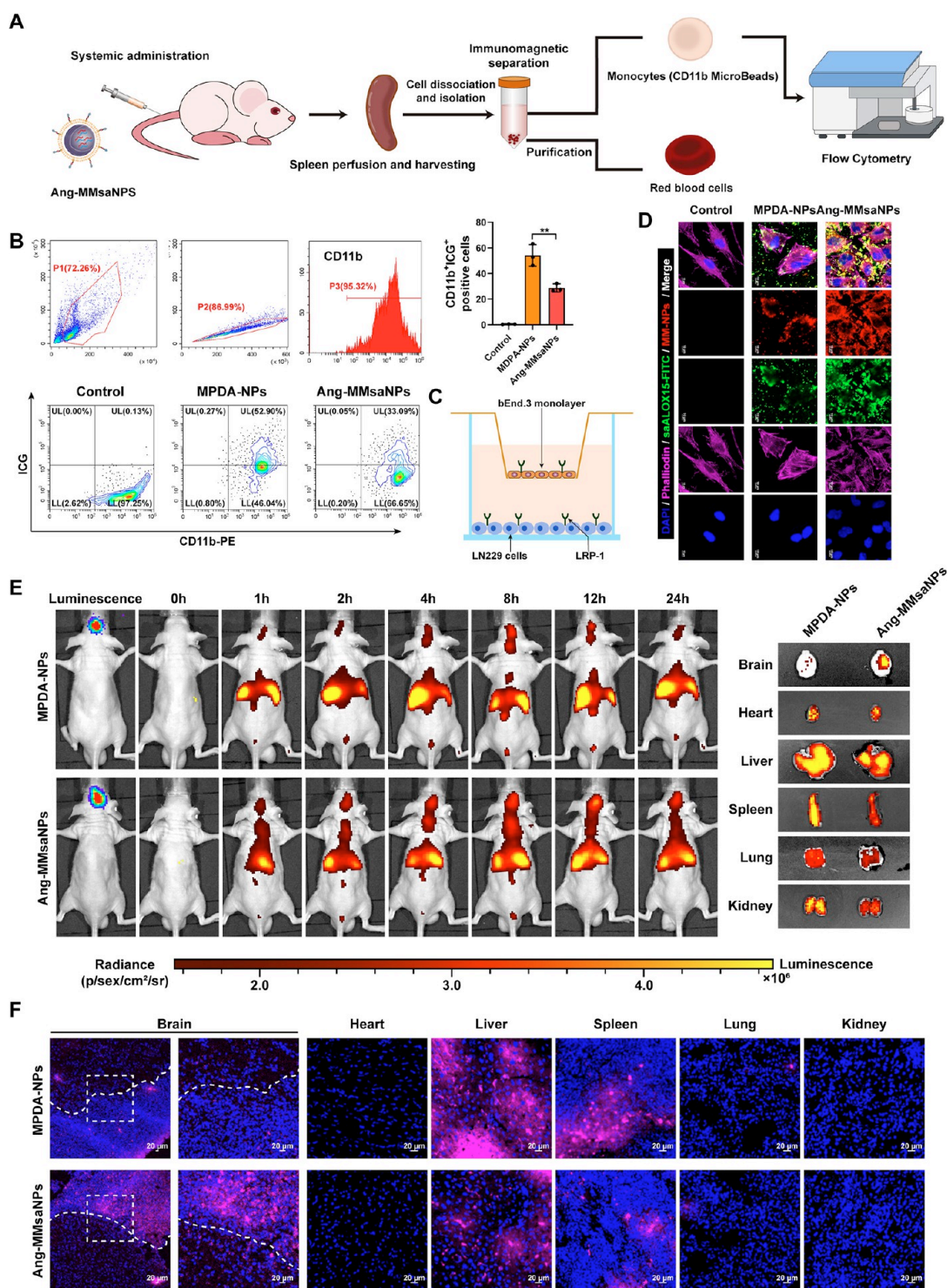


Figure 5. Ang-MMsaNPs escape the MPS and effectively target and accumulate in GBM. (A) Schematic image. Process of Ang-MMsaNPs animal tail vein injection, spleen harvesting, immunomagnetic separation, monocytes isolation, and flow cytometry sorting. (B) The levels of ICG positivity in CD11b⁺ monocytes were measured after Ang-MMsaNPs treatment by flow cytometry. (C) Schematic image of the BBB model in vitro. (D) Immunofluorescence images detected MPDA-NPs and Ang-MMsaNPs uptake into LN229 cells after passing through a bEnd.3 monolayer. Scale bar, 10 μm. (E) Fluorescence images of orthotopic LN229-bearing nude mice and major organs following injection of ICG-labeled MPDA-NPs and Ang-MMsaNPs. (F) ICG-labeled NPs fluorescence from major organs in orthotopic mice model after intravenous injection of different types of NPs.

time oxygen consumption rate (OCR), an indicator of the mitochondrial OXPHOS rate, was directly measured by using a Seahorse XF extracellular flux analyzer. After Ang-MMsaNPs treatment, GBM cells treated with Ang-MMsaNPs exhibited

obvious respiratory suppression at the basal level, maximal respiratory capacity, and nonmitochondrial respiration coupled with oxidative respiration in LN229 cells, suggesting profound mitochondrial dysfunction triggered by the Ang-MMsaNPs

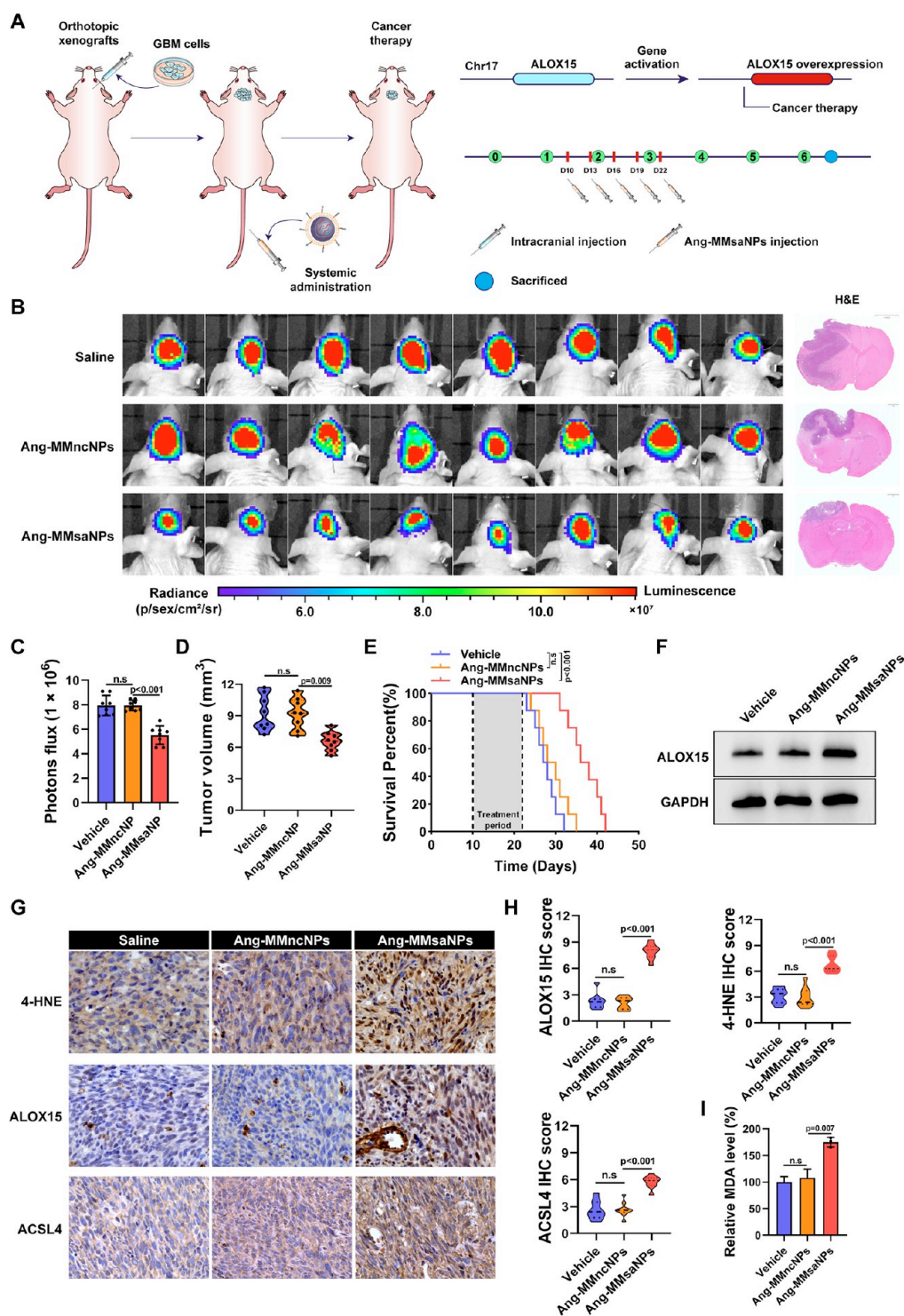


Figure 6. The in vivo therapeutic efficacy of Ang-MMsaNPs in orthotopic GBM-bearing mice. (A) Schematic image. Timeline of the LN229 orthotopic tumor model receiving NPs therapy. (B, C) Luciferase luminescence levels of mice following the indicated treatments. (D) Tumor volume quantification after the last treatment. (E) Survival curves of LN229-bearing mice following the indicated treatments. $n = 8$ animals per treatment group. (F) Western blot was used to detect the overexpression efficiency of saALOX15 in tumor cells after NPs treatment. (G, H) IHC analysis of ALOX15, ACSL4 and 4-HNE expression in tumor tissues after NPs treatment. (I) The expression level of MDA in tumor tissues after NPs treatment.

(Figure 4H). The vast majority of ATP is produced in mitochondria, and Ang-MMsaNPs treatment inhibited ATP production (Figure 4I). To further validate the relationship between mitochondria dysfunction and Ang-MMsaNP-induced ferroptosis, we used a mitochondrion-targeted antioxidant

(Mito-TEMPO), and we found that Mito-TEMPO alleviated Ang-MMsaNP-induced ferroptotic cell death and lipid peroxidation (Supplementary Figure S9). These findings demonstrated that Ang-MMsaNPs induced GBM ferroptosis by promoting mitochondrial damage.

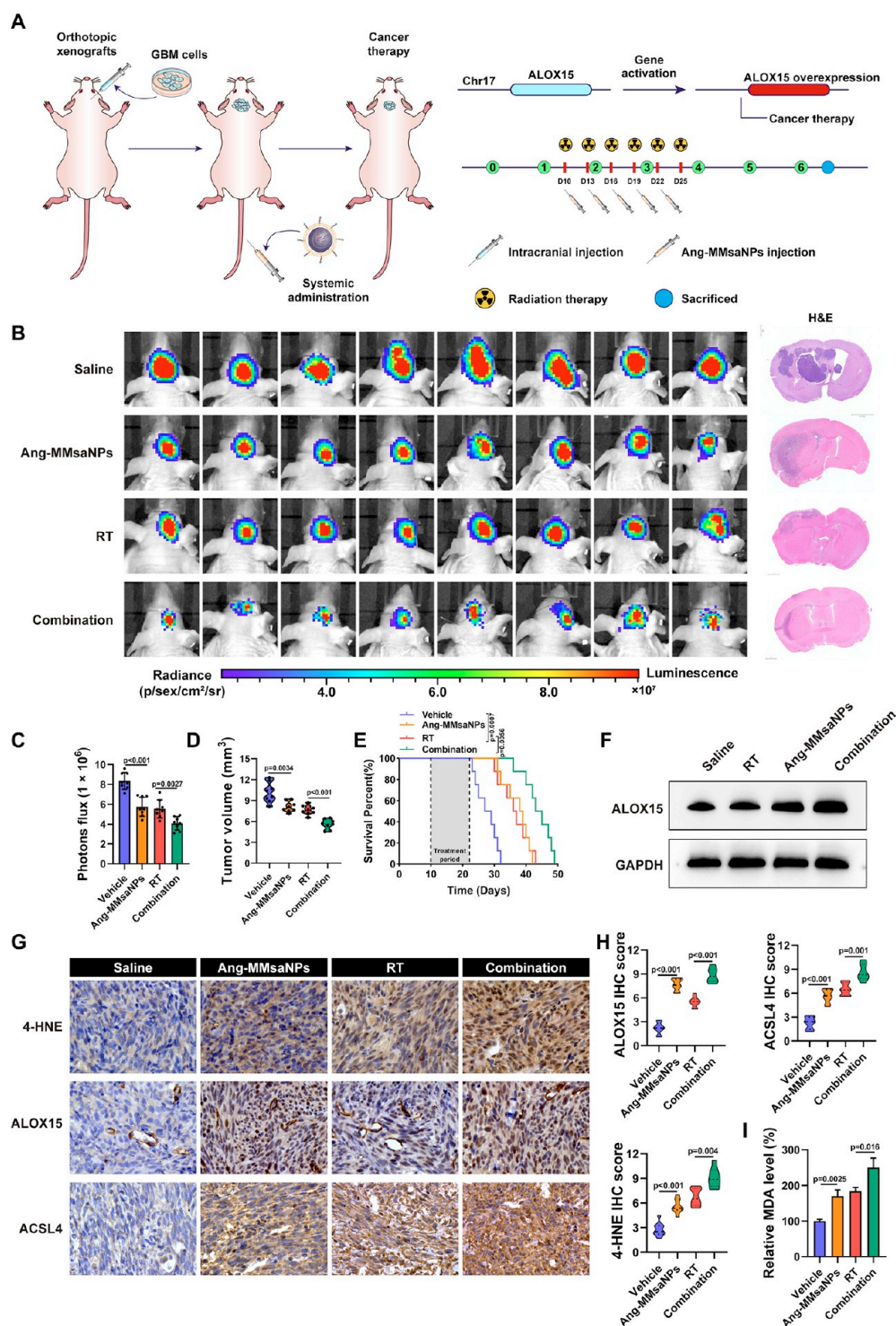


Figure 7. The combination of Ang-MMsNPs and RT is efficient for tumor regression in GBM. (A) Schematic image. Timeline of the LN229 orthotopic tumor model receiving combination therapy. (B, C) Luciferase luminescence levels of mice following the indicated treatments. (D) Tumor volume quantification after the last treatment. (E) Survival curves of LN229-bearing mice following the indicated treatments. $n = 8$ animals per treatment group. (F) Western blot was used to detect the overexpress efficiency of saALOX15 in tumor cells after combination treatment. (G, H) IHC analysis of ALOX15, ACSL4 and 4-HNE expression in tumor tissues after combination treatment. (I) The expression level of MDA in tumor tissues after combination treatment.

Enhanced Tumor Targeting of Ang-MMsNPs via Mononuclear Phagocytic System Escape and Decorated with a Targeting Peptide. Increasing evidence demonstrated that MM-coated nanoparticles inhibit phagocytosis via the MPS.¹⁹ The cellular phagocytosis of Ang-MMsNPs was

evaluated in the RAW264.7 cells. Confocal laser microscopy images showed that both indocyanine green (ICG)-labeled MPDA-NPs and Ang-MMsNPs were internalized by macrophages in a time-dependent manner. However, after internalization by the macrophages, much more intense red fluorescence

emitted by the MPDA-NPs was detected than that emitted from the Ang-MMsaNPs at the same time (Supplementary Figure S10). To explore whether Ang-MMsaNPs escape phagocytosis mediated by the MPS and thereby show increased tumor-targeting specificity *in vivo*, ICG-labeled MPDA-NPs and Ang-MMsaNPs were injected into mice via the tail vein (Figure 5A). Generally, dead cells, cellular debris, and foreign particles are cleared through efficient phagocytosis by the circulating monocytes and other cells. CD11b⁺ monocytes from the blood of control (untreated) mice showed baseline ICG positivity. A decrease in the number of circulating ICG⁺ monocytes (indicative of phagocytosis) was observed when the mice were treated with Ang-MMsaNPs compared to MPDA-NPs, supporting the idea that the MM on the NPs limits their clearance (Figure 5B).

Angiopoietin-2 (Ang) can specifically bind to the lipoprotein receptor-related protein 1 (LRP1) receptor, enhance the transport efficiency of NP across the BBB, and deliver drugs to the glioma.^{20–23} In addition, the overexpression of $\alpha 4$ or $\beta 1$ integrin on the surface of macrophages can bind vascular cell adhesion molecule-1 (VCAM-1), promote the penetration of the BBB and target gliomas.²⁴ To assess the ability of Ang-MMsaNPs to permeate the BBB, an *in vitro* model was established with Transwell inserts placed in 24-well plates. bEnd.3 cells were cultured in the upper Transwell compartment, while LN229 cells were seeded in the bottom compartment. Cy3-labeled MM-NPs (saALOX15 labeled with FITC) were added to the upper with the bEnd.3 cells with minimum shaking for 24 h (Figure 5C). Analysis via confocal microscopy demonstrated that Ang-MMsaNPs showed significantly more efficient BBB permeation and a greater ability to target LN229 cells than the MPDA-NPs (Figure 5D and Supplementary Figure S11). To detect the targeted delivery of Ang-MMsaNPs to specific organs, we injected ICG-labeled MPDA-NPs or Ang-MMsaNPs into the tail vein of mice. Orthotopic LN229-Luc tumor-bearing immunocompromised mice injected with Ang-MMsaNPs exhibited strong ICG fluorescence in the tumor within 1 h, and the emission steadily increased to a maximum at 12 h with fluorescence maintained up to 24 h, indicating efficient BBB penetration and tumor accumulation and retention. Compared with that of the MPDA-NPs, the distribution of Ang-MMsaNPs in the liver, lung, heart, kidney, and spleen was significantly reduced, and the distribution in the brain was significantly increased (Figure 5E and Supplementary Figure S12). This result confirms that NPs coated with MM reduced the accumulation of NPs in the main organs *in vivo*, reducing the nonspecific toxicity and side effects of the MM-coated NPs. Most importantly, there is increased intratumoral distribution, as shown by *ex vivo* imaging. The results of confocal image analysis of organ tissue sections are consistent with the *in vitro* fluorescence imaging data (Figure 5F). Collectively, Ang-MMsaNPs showed the ability to effectively target and accumulate in gliomas due to their long-term circulation and specific interactions with glioma, which can be attributed to the macrophage-mimicking tumor-tropism feature and targeting peptide of the NPs.

In Vivo Therapeutic Efficacy of Ang-MMsaNPs in Orthotopic GBM Mice. To evaluate the therapeutic potential of Ang-MMsaNPs for GBM treatment, we needed to address two major safety concerns about nanocapsule therapeutics: their potential toxicity and immunogenicity. Routine blood tests demonstrated that mice treated with Ang-MMsaNPs or PBS showed similar levels of red blood cells (RBCs), white blood

cells (WBCs), platelets (PLTs), creatinine (Cr), uric acid (UA), alanine aminotransferase (ALT), alkaline phosphatase (ALP), aspartate aminotransferase (AST), serum albumin (ALB) and body weight, indicating that Ang-MMsaNPs induce negligible toxic effects on the liver or hematological factors (Supplementary Figure S13). Together, these results indicate that Ang-MMsaNPs cause very few safety concerns.

Next, we evaluated whether the activation of ALOX15 mediated by Ang-MMsaNPs observed *in vitro* can be translated to therapeutic efficacy *in vivo*. Orthotopic GBM-bearing mice were randomly divided into groups and injected with intravenous tail vein injections of Ang-MMsaNPs, Ang-MMncNPs, or PBS every 3 days, and tumor growth was evaluated by using *in vivo* bioluminescence imaging (Figure 6A). The mice treated with Ang-MMsaNPs displayed the smallest tumor volume and the weakest bioluminescence intensity, whereas other groups showed no obvious inhibitory effects (Figure 6B–D). Furthermore, compared with those of other groups, the survival of the mice treated with Ang-MMsaNPs was significantly prolonged (Figure 6E). Immunoblot demonstrated a significant increase in the level of ALOX15 protein expression in the Ang-MMsaNP-treated cohort but not in the control treatment groups (Figure 6F). The staining for 4-HNE and ACSL4 was significantly increased after Ang-MMsaNPs treatment, suggesting that Ang-MMsaNPs increased the lipid peroxidation rate of the tumor xenograft samples (Figure 6G,H). Consistent with the increased levels of 4-HNE and ACSL4 in the Ang-MMsaNPs group, overexpression of ALOX15 resulted in increased MDA levels, suggesting the most potent ferroptosis induction in this group (Figure 6I). These data successfully confirmed that the biomimetic NPs showed good safety after long-term administration in mice without causing any obvious side effects and the notable efficacy of Ang-MMsaNPs, which promoted ferroptosis in the tumors of orthotopic GBM-bearing mice.

Combinatorial Treatment Results in Synergistic Tumor Regression *In Vivo*. Although RT is the mainstay of GBM treatment, radiotherapy resistance is still the main factor leading to radiotherapy failure. Subsequently, we detected the therapeutic effect of Ang-MMsaNPs combined with RT in a GBM orthotopic mouse model (Figure 7A). Bioluminescence imaging showed that tumor growth was inhibited to varying degrees after various treatments compared with that in the PBS-treated control group (Figure 7B). Ang-MMsaNP-treated group showed noticeable inhibition of tumor growth compared with the PBS group. When Ang-MMsaNPs and RT were combined for treatment, the tumor volume in the combination group was significantly smaller than in the single-agent Ang-MMsaNPs or RT group (Figure 7C,D). Compared to Ang-MMsaNPs or RT monotherapy, the combination therapy resulted in a significant delay in tumor progression and prolonged overall survival (Figure 7E). These data effectively confirmed the notable efficacy of Ang-MMsaNPs in synergy with RT. Importantly, Ang-MMsaNPs treatment promoted ALOX15 expression, and Ang-MMsaNPs combined with RT treatment further increased ALOX15 levels in tumor samples (Figure 7F). A pathological analysis of ACSL4 expression and 4-HNE via an IHC assay was performed to detect any ferroptotic events in GBM orthotopic mode. We observed that RT or Ang-MMsaNPs treatment led to an increased ferroptosis rate in GBM cells, as measured by ACSL4 and 4-HNE staining intensity and MDA level (Figure 7G–I). These data suggest that the RT + Ang-MMsaNPs combination treatment is more effective than other treatments in orthotopic GBM models.

DISCUSSION

Numerous studies have substantiated the potential value of targeting ferroptosis in the treatment of multiple cancer types.²⁵ The recent determination that RT has the potential to trigger ferroptosis further supports the promise of ferroptosis-inducing therapeutic agents.¹⁰ Despite the potential benefits of ferroptosis inducers, several challenges limit their clinical application. These challenges include complex pharmacokinetics and biodistribution, compromised selectivity for cancer cells, limited understanding of ferroptosis mechanisms, few ferroptotic biomarkers, and early stage clinical development.²⁶ Additional investigation is required to tackle these obstacles and bolster the progress of ferroptosis stimulators as efficient and secure anticancer therapies.

Large-scale CRISPR loss-of-function genomic screening is an effective and unbiased strategy for identifying genes and pathways involved in tumorigenesis.²⁷ In our study, we performed a series of CRISPR–Cas9 knockout library screens combined with RNA-seq and clinical data analysis to identify ALOX15 as a crucial lipid peroxidation enzyme. RNA-seq analysis showed that ALOX15 is closely related to the regulation of ferroptosis, and overexpression of ALOX15 led to an increased expression of ferroptosis-related genes in GBM cells. Our research has revealed a significant correlation between decreased ALOX15 expression and unfavorable prognosis in glioma patients across various data sets, including those in the TCGA, Gravendeel, and Rembrandt databases and glioma tissue microarray data. Furthermore, accumulating evidence suggests that the level of ALOX15 and its metabolites is reduced in many human cancers, including lung, breast, colorectal, and pancreatic cancers.^{28–30} Re-expression of ALOX15 in human cancer cells using protein kinase G activator or plasmids and adenoviral vectors inhibited the proliferation of these cells both *in vivo* and *in vitro*, indicating that ALOX15 is a tumor suppressor.²⁸

RNAa is a recently discovered small double-stranded RNA (dsRNA)-mediated gene regulatory mechanism that targets gene regulatory sequences and involves transcriptional and epigenetic changes.³¹ Despite the presence of several unanswered questions, there is mounting evidence indicating that RNAa is not only an approach to investigating gene function and regulation but also holds promise as a potential treatment method for clinical translation against cancers. MTL-CEBPA, a first-in-class compound that reverses CEBPA downregulation in oncogenic processes via the action of CEBPA-51 saRNA and is currently in clinical trials for the treatment of hepatocellular carcinoma.³² To activate the expression of ALOX15 *in vitro* and *in vivo*, we identified a specific sequence (saALOX15) capable of activating the ALOX15 expression. We demonstrated that saALOX15 actively facilitated ferroptosis through the rapid amplification of lipid peroxidation, until the toxic products reached lethal levels. Nucleic acid drugs, such as antisense oligonucleotides, RNAi agents, and aptamers, have shown great promise as therapeutic agents for various diseases, including genetic disorders and cancers. However, there are several limitations to their clinical application. The most important of these limitations stems from the challenge of delivering nucleic acid drugs to target cells and tissues because of their large size, hydrophilicity, and susceptibility to enzymatic and nuclease degradation.³³ Thus, the development of efficient and safe delivery systems and strategies is critical for achieving therapeutic efficacy while minimizing off-target effects.

NPs camouflaged by biological cell membranes have recently been the focus of attention due to their prolonged circulation *in vivo*.¹⁴ Their innate self-recognition features optimize their dynamic properties by camouflaging the contents to evade the elimination of the MPS and the immunological surveillance.¹⁶ The membrane camouflage strategy has led to an increased half-life of NPs in systemic circulation and thus increases the ability of the drugs to adhere to tumors without loss of the drug load capacity or its nanosize advantage. We developed an MM biomimetic nanoplatform based on MPDA coloaded with saALOX15 and a targeted ligand that crossed the BBB to achieve orthotopic GBM targeting. Ang-MMsaNPs showed good *in vivo* and *in vitro* targeting, significantly delayed the progression of GBM in mice, and enhanced the effects of RT.

CONCLUSION

In conclusion, our study systematically identified ALOX15 as a key driver of ferroptosis in GBM cells using an unbiased genome-wide CRISPR–Cas9 knockout screening pool. Furthermore, the saRNA-mediated activation of ALOX15 facilitates ferroptosis through rapid amplification of lipid peroxidation to produce lethal levels of toxins. We also developed MM-coated saALOX15-loaded MPDA NPs, Ang-MMsaNPs that target glioma. Ang-MMsaNPs exhibit immunological camouflage that allows the NPs to avoid phagocytosis by the MPS and to promote the uptake of NPs by GBM, thereby promoting the ferroptosis of GBM cells. By investigating the underlying molecular mechanisms, we found that Ang-MMsaNPs induced mitochondrial dysfunction and acquisition of an abnormal mitochondrial morphology. In particular, *in vivo* treatment results illustrated that Ang-MMsaNPs significantly delayed the progression of GBM and enhanced the effects of RT. Finally, the biomimetic nanoparticles showed a good safety profile and did not cause any significant side effects, even when administered to mice for a long period. Therefore, Ang-MMsaNPs are a potential nanocarrier and are expected to become effective targeted drug delivery systems for the treatment of GBM.

EXPERIMENTAL SECTION

Cell Lines. Human GBM cell lines LN229, mouse RAW264.7 macrophages, mouse endothelial cells (bEnd.3), and HEK293T cell line were obtained from ATCC and were cultured in Dulbecco's Modified Eagle Medium (DMEM) containing with 10% FBS and 1% penicillin/streptomycin at 37 °C with 5% CO₂. All cells were checked for mycoplasma. RSL3 for constructing RSL3-resistant cell lines were obtained from TargetMol.

Genome-Wide CRISPR Screen. The CRISPR screening was performed as described previously.¹² Briefly, the genome-wide CRISPR/Cas9 knockout library was infected into LN229 cells at a low multiplicity of infection (MOI ~ 0.3). This library uses the LentiCRISPR version 2 core vector from Feng Zhang (Addgene).

Western Blot. Cells were digested through conventional digestion to get precipitates, and were lysed in Western and IP lysis buffer (NCM) containing protease and phosphatase inhibitor cocktails (Proteintech) on ice for 1 h. Then, protein concentration was quantified by BCA assay (Thermo Fisher). After boiling with loading buffer, equal amounts of samples were run on SDS-PAGE and transferred to PVDF membranes (EMD Millipore). Subsequently, the membranes were subjected to overnight incubation with primary antibodies at a temperature of 4 °C. We then meticulously cleansed the membranes three times, proceeded with incubation using a secondary antibody for 1 h at room temperature, and again cleaned it three times.

Immunofluorescence. Cells grown in a 20 mm Glass Bottom Cell Culture Dish or histologic section were washed 3 times with PBS, then the tissue samples were immersed in a 4% paraformaldehyde solution

for a duration of 20 min. Following this, the samples underwent three washes with PBS and were subsequently treated with 0.5% Triton X-100 to promote permeabilization at room temperature for a period of 30 min. After another three washes with PBS, the samples were subjected to an overnight incubation at 4 °C with primary antibodies, following a 40 min blocking step using 5% BSA. To visualize the targeted molecules, the samples were incubated with fluorescent secondary antibodies for 1 h and then washed three times with PBS. Finally, a 1 min incubation with DAPI was performed to stain the cell nucleus.

ROS and Lipid Peroxidation Assay. Cells were seeded in 6-well plates with a Glass Bottom (NEST, China) and subjected to different treatments. The C11 BODIPY 581/591 assay kit (Dojindo, Japan) and Reactive Oxygen Species Assay Kit (Dojindo, Japan) were used following the manufacturer's manual, respectively. Results were analyzed by flow cytometry using a Beckman CytoFLEX.

Transmission Electron Microscopy. Cells were seeded in 75 cm² flasks washed 3 times with PBS, and then used 2.5% glutaraldehyde soaking treatment for 5 min in the dark. 1×10^7 cells were harvested with a cell scraper, and fixed with 2.5% glutaraldehyde at 4 °C for 2 h in the dark. After dehydration and embedding, samples were incubated at 60 °C for 48 h. Transmission electron microscopy was performed after double staining with uranyl acetate and lead citrate.

RiboGreen Assay. Quant-iT RiboGreen RNA Kit (Ribobio, China) is used to test the encapsulation efficiency according to the manufacturer's manual.

Establishment of PDOs. PDOs were established and cultivated as described previously.³⁴

In Vitro BBB Model. bEnd.3 cells were cultured in the upper chamber of Transwell inserts, while LN229 cells were cultured in the lower chamber for 7 days in DMEM supplemented with 10% FBS. This created a membrane that acts as a blood–brain barrier.

Measurement of Mitochondrial Lipid Peroxidation. Cells were grown in a 20 mm Glass Bottom Cell Culture Dish (Corning, USA) and treated with irradiation or drugs. MitoPeDPP assay kit (Dojindo, Japan) to measure the mitochondrial lipid peroxidation and MitoBright LT Deep Red assay kit (Dojindo, Japan) to observe mitochondrial morphology; the assay kits were used following the manufacturer's manual.

Preparation of the Macrophage Membranes. Ang-over-expressing adenovirus with membrane localization signal was used to infect RAW264.7 cells. RAW264.7 cell membranes were extracted by using a membrane protein extraction kit. Briefly, harvested cells were dispersed in a buffer for extracting membrane proteins and cooled in an ice bath for 15 min. The cell suspension was then transferred to a glass homogenizer and homogenized about 30 times. The obtained mixture was subsequently centrifuged to obtain the cell membranes. The harvested cells were dispersed in a buffer for extracting membrane proteins and cooled in an ice bath for 15 min. The cell suspension was then transferred to a glass homogenizer and homogenized for about 30 times. The resulting mixture was subsequently centrifuged to acquire the cell membranes.

Preparation of MM Camouflaged MPDA-saNPs (Ang-MMsaNPs). Ang-MMsaNPs were prepared by coating MM on the surface of MPDA by direct extrusion. Briefly, MM and MPDA vesicles were mixed at a 1:1 (w/w) ratio of membrane protein to polymer and sonicated for 3 min in an ultrasonic bath. The mixture was then extruded 8 times through a 0.2 μm porous polycarbonate membrane using an Avestin microextruder to collect Ang-MMsaNPs.

Characterization of the Nanoparticles. A Malvern Zetasizer Nano ZS instrument (Nano ZS, UK) was used to analyze the size distribution and zeta potential of MPDA-NPs and Ang-MMsaNPs. NP solutions at a concentration of 100 μg/mL were dropped onto carbon-coated grids and stained with 1% phosphotungstic acid. TEM was used to observe the morphology of MPDA-NPs and Ang-MMsaNPs. of 200 kV.

Measurement of Oxygen Consumption Rate (OCR). Cellular oxidative respiration was measured by Seahorse XF Bioenergetic Assay using a Seahorse Cell Mito Stress Assay Kit (Seahorse Bioscience, North Billerica, MA, USA). In brief, LN229 cells were seeded onto an

XFp microplate. After 1 day of incubation, the medium was changed to DMEM without sodium bicarbonate and supplemented with 2% fetal bovine serum. OCR was measured at steady state, followed by the sequential addition of oligomycin (1 μM), carbonyl cyanide-4-[trifluoromethoxy]phenylhydrazone (FCCP; 0.5 μM), rotenone (0.5 μM), and imidazole (1 μM). Add the mixture to the wells and determine maximal and nonmitochondrial respiration rates according to the manufacturer's instructions.

Determination of ATP and Malondialdehyde (MDA) Levels. The fluorometric assay kit (Beyotime, S0026) was utilized to quantify the ATP concentration. Evaluation of the MDA concentration was performed using a Lipid Peroxidation MDA Assay Kit (Beyotime, S0131).

Sorting of CD11b Positive Monocytes. CD11b⁺ cells were isolated from a single-cell suspension of the mouse spleen using CD11b MicroBeads UltraPure, one MS Column, and a MiniMACS Separator. Cells were labeled with CD11b-PE and analyzed by using flow cytometry.

Orthotopic Mouse Xenografts. GBM cells expressing luciferase were digested through conventional digestion to obtain white precipitates and suspended with normal saline, and then the cells were intracranially transplanted into immunocompromised mice by using stereotaxic apparatus, exposed to the skull, and three-dimensional coordinates were established around bregma; a 0.7 mm diameter drill was used to drill a hole 2.5 mm to the left of the sagittal suture and 0.5 mm near the suture, and the injection depth was 2.5 mm.

Bioluminescence Imaging (BLI). Administration of the luciferin substrate: The luciferase substrate, typically D-luciferin, is administered to the animal via intraperitoneal injection, oral gavage, or inhalation. After a short period for luciferin to distribute throughout the animal's body, the animal is placed in the imaging chamber of a sensitive camera (e.g., IVIS system). The camera captured the emitted photons from the luciferase reaction, generating a bioluminescent image of the animal. The acquired images are quantified using specialized software to calculate the intensity and location of bioluminescent signals.

Histology and Immunohistochemistry. Collected mouse tissues were fixed in 4% paraformaldehyde in PBS buffer overnight. They were then gradually dehydrated in ethanol, transferred to xylene, and embedded in paraffin. Paraffin-embedded tissues were cut into 4 μm thick sections and histologically examined by H&E staining and immunohistochemistry.

Statistical Analyses. Results from cell culture experiments were obtained from a minimum of 3 independent replicates. The data are presented as the mean ± standard deviation (SD). To compare differences between groups, a two-tailed unpaired Student's *t* test was performed. A *p*-value less than 0.05 was considered statistically significant (**p* < 0.05, ***p* < 0.01, ****p* < 0.001, *****p* < 0.0001).

ASSOCIATED CONTENT

Data Availability Statement

All data generated or analyzed during the course of this research will be included in the published article, or upon reasonable request from the relevant authors.

Supporting Information

The Supporting Information is available free of charge at <https://pubs.acs.org/doi/10.1021/acsnano.3c07555>.

Supplementary experimental agents, saRNA sequences, and supplementary figures (PDF)

AUTHOR INFORMATION

Corresponding Authors

Donghui Han – Department of Urology, Xijing Hospital, Xi'an 710032, China; Email: 906812205@qq.com

Meng Li – State Key Laboratory of Cancer Biology, Biotechnology Center, School of Pharmacy, The Fourth

Military Medical University, Xi'an 710032, China;
Email: limeng@fmmu.edu.cn

Jintao Gu – State Key Laboratory of Cancer Biology,
Biotechnology Center, School of Pharmacy, The Fourth
Military Medical University, Xi'an 710032, China;
Email: gujintao@fmmu.edu.cn

Authors

Zhengcong Cao – State Key Laboratory of Cancer Biology,
Biotechnology Center, School of Pharmacy, The Fourth
Military Medical University, Xi'an 710032, China

Xiao Liu – Department of Neurosurgery, Xijing Hospital, Xi'an
710032, China; orcid.org/0000-0003-1490-3836

Wangqian Zhang – State Key Laboratory of Cancer Biology,
Biotechnology Center, School of Pharmacy, The Fourth
Military Medical University, Xi'an 710032, China

Keying Zhang – Department of Urology, Xijing Hospital, Xi'an
710032, China

Luxiang Pan – State Key Laboratory of Cancer Biology,
Biotechnology Center, School of Pharmacy, The Fourth
Military Medical University, Xi'an 710032, China

Maorong Zhu – State Key Laboratory of Cancer Biology,
Biotechnology Center, School of Pharmacy, The Fourth
Military Medical University, Xi'an 710032, China

Haozhe Qin – State Key Laboratory of Cancer Biology,
Biotechnology Center, School of Pharmacy, The Fourth
Military Medical University, Xi'an 710032, China

Cheng Zou – State Key Laboratory of Cancer Biology,
Biotechnology Center, School of Pharmacy, The Fourth
Military Medical University, Xi'an 710032, China

Weizhong Wang – Department of Neurosurgery, Xijing
Hospital, Xi'an 710032, China

Cong Zhang – Department of Radiation Oncology, Xijing
Hospital, Xi'an 710032, China

Yalong He – Department of Neurosurgery, Xijing Hospital,
Xi'an 710032, China

Wei Lin – Department of Neurosurgery, Xijing Hospital, Xi'an
710032, China

Yingqi Zhang – State Key Laboratory of Cancer Biology,
Biotechnology Center, School of Pharmacy, The Fourth
Military Medical University, Xi'an 710032, China

Complete contact information is available at:

<https://pubs.acs.org/10.1021/acsnano.3c07555>

Author Contributions

[#]Z.C., X.L., W.Z., and K.Z. contributed equally to this work

Notes

The authors declare no competing financial interest.

ACKNOWLEDGMENTS

This work was supported by the National Natural Science Foundation of China (82003220). This study was approved by the FMMU Ethics Committee (Xian, China).

REFERENCES

- (1) Gu, J.; Mu, N.; Jia, B.; Guo, Q.; Pan, L.; Zhu, M.; Zhang, W.; Zhang, K.; Li, W.; Li, M.; Wei, L.; Xue, X.; Zhang, Y.; Zhang, W. Targeting radiation-tolerant persister cells as a strategy for inhibiting radioresistance and recurrence in glioblastoma. *Neuro Oncol* **2022**, *24* (7), 1056–1070.
- (2) Liu, T.; Zhu, C.; Chen, X.; Guan, G.; Zou, C.; Shen, S.; Wu, J.; Wang, Y.; Lin, Z.; Chen, L.; Cheng, P.; Cheng, W.; Wu, A. Ferroptosis, as the most enriched programmed cell death process in glioma, induces

immunosuppression and immunotherapy resistance. *Neuro Oncol* **2022**, *24* (7), 1113–1125.

(3) Quail, D. F.; Joyce, J. A. The Microenvironmental Landscape of Brain Tumors. *Cancer Cell* **2017**, *31* (3), 326–341.

(4) Tang, W.; Fan, W.; Lau, J.; Deng, L.; Shen, Z.; Chen, X. Emerging blood-brain-barrier-crossing nanotechnology for brain cancer therapeutics. *Chem. Soc. Rev.* **2019**, *48* (11), 2967–3014.

(5) Sampson, J. H.; Gunn, M. D.; Fecci, P. E.; Ashley, D. M. Brain immunology and immunotherapy in brain tumours. *Nat. Rev. Cancer* **2020**, *20* (1), 12–25.

(6) Lei, G.; Zhang, Y.; Koppula, P.; Liu, X.; Zhang, J.; Lin, S. H.; Ajani, J. A.; Xiao, Q.; Liao, Z.; Wang, H.; Gan, B. The role of ferroptosis in ionizing radiation-induced cell death and tumor suppression. *Cell Res.* **2020**, *30* (2), 146–162.

(7) Liang, C.; Zhang, X.; Yang, M.; Dong, X. Recent Progress in Ferroptosis Inducers for Cancer Therapy. *Adv. Mater.* **2019**, *31* (51), No. e1904197.

(8) Chen, Y.; Li, L.; Lan, J.; Cui, Y.; Rao, X.; Zhao, J.; Xing, T.; Ju, G.; Song, G.; Lou, J.; Liang, J. CRISPR screens uncover protective effect of PSTK as a regulator of chemotherapy-induced ferroptosis in hepatocellular carcinoma. *Mol. Cancer* **2022**, *21* (1), 11.

(9) Mou, Y.; Wang, J.; Wu, J.; He, D.; Zhang, C.; Duan, C.; Li, B. Ferroptosis, a new form of cell death: opportunities and challenges in cancer. *J. Hematol. Oncol.* **2019**, *12* (1), 34.

(10) Su, Y.; Zhao, B.; Zhou, L.; Zhang, Z.; Shen, Y.; Lv, H.; AlQudsy, L. H. H.; Shang, P. Ferroptosis, a novel pharmacological mechanism of anti-cancer drugs. *Cancer Lett.* **2020**, *483*, 127–136.

(11) Mengwasser, K. E.; Adeyemi, R. O.; Leng, Y.; Choi, M. Y.; Clairmont, C.; D'Andrea, A. D.; Elledge, S. J. Genetic Screens Reveal FEN1 and APEX2 as BRCA2 Synthetic Lethal Targets. *Mol. Cell* **2019**, *73* (5), 885–899.

(12) Du, M.; Gu, J.; Liu, C.; Liu, N.; Yu, Z.; Zhou, C.; Heng, W.; Cao, Z.; Wei, F.; Zhu, K.; Wang, Y.; Zhang, W.; Xue, X.; Zhang, Y.; Qian, J. Genome-wide CRISPR screen identified Rad18 as a determinant of doxorubicin sensitivity in osteosarcoma. *J. Exp. Clin. Cancer Res.* **2022**, *41* (1), 154.

(13) Li, J.; Wu, Y.; Wang, J.; Xu, X.; Zhang, A.; Li, Y.; Zhang, Z. Macrophage Membrane-Coated Nano-Gemcitabine Promotes Lymphocyte Infiltration and Synergizes AntiPD-L1 to Restore the Tumoricidal Function. *ACS Nano* **2023**, *17* (1), 322–336.

(14) Xiao, T.; He, M.; Xu, F.; Fan, Y.; Jia, B.; Shen, M.; Wang, H.; Shi, X. Macrophage Membrane-Camouflaged Responsive Polymer Nanogels Enable Magnetic Resonance Imaging-Guided Chemotherapy/Chemodynamic Therapy of Orthotopic Glioma. *ACS Nano* **2021**, *15* (12), 20377–20390.

(15) Cao, H.; Dan, Z.; He, X.; Zhang, Z.; Yu, H.; Yin, Q.; Li, Y. Liposomes Coated with Isolated Macrophage Membrane Can Target Lung Metastasis of Breast Cancer. *ACS Nano* **2016**, *10* (8), 7738–48.

(16) Zhang, Y.; Cai, K.; Li, C.; Guo, Q.; Chen, Q.; He, X.; Liu, L.; Zhang, Y.; Lu, Y.; Chen, X.; Sun, T.; Huang, Y.; Cheng, J.; Jiang, C. Macrophage-Membrane-Coated Nanoparticles for Tumor-Targeted Chemotherapy. *Nano Lett.* **2018**, *18* (3), 1908–1915.

(17) Li, Y.; Liu, Y.; Ren, Y.; Su, L.; Li, A.; An, Y.; Rotello, V.; Zhang, Z.; Wang, Y.; Liu, Y.; Liu, S.; Liu, J.; Laman, J. D.; Shi, L.; van der Mei, H. C.; Busscher, H. J. Coating of a Novel Antimicrobial Nanoparticle with a Macrophage Membrane for the Selective Entry into Infected Macrophages and Killing of Intracellular Staphylococci. *Adv. Funct. Mater.* **2020**, *30* (48), No. 2004942.

(18) Zheng, L.; Wang, L.; Gan, J.; Zhang, H. RNA activation: promise as a new weapon against cancer. *Cancer Lett.* **2014**, *355* (1), 18–24.

(19) Lai, J.; Deng, G.; Sun, Z.; Peng, X.; Li, J.; Gong, P.; Zhang, P.; Cai, L. Scaffolds biomimicking macrophages for a glioblastoma NIR-Ib imaging guided photothermal therapeutic strategy by crossing Blood-Brain Barrier. *Biomaterials* **2019**, *211*, 48–56.

(20) Chen, H.; Li, T.; Liu, Z.; Tang, S.; Tong, J.; Tao, Y.; Zhao, Z.; Li, N.; Mao, C.; Shen, J.; Wan, M. A nitric-oxide driven chemotactic nanomotor for enhanced immunotherapy of glioblastoma. *Nat. Commun.* **2023**, *14* (1), 941.

- (21) Khan, N. U.; Ni, J.; Ju, X.; Miao, T.; Chen, H.; Han, L. Escape from abluminal LRP1-mediated clearance for boosted nanoparticle brain delivery and brain metastasis treatment. *Acta Pharm. Sin B* **2021**, *11* (5), 1341–1354.
- (22) Jiang, Y.; Yang, W.; Zhang, J.; Meng, F.; Zhong, Z. Protein Toxin Chaperoned by LRP-1-Targeted Virus-Mimicking Vesicles Induces High-Efficiency Glioblastoma Therapy In Vivo. *Adv. Mater.* **2018**, *30* (30), No. e1800316.
- (23) Guo, Q.; Zhu, Q.; Miao, T.; Tao, J.; Ju, X.; Sun, Z.; Li, H.; Xu, G.; Chen, H.; Han, L. LRP1-upregulated nanoparticles for efficiently conquering the blood-brain barrier and targetedly suppressing multifocal and infiltrative brain metastases. *J. Controlled Release* **2019**, *303*, 117–129.
- (24) Cheng, V. W. T.; de Pennington, N.; Zakaria, R.; Larkin, J. R.; Serres, S.; Sarkar, M.; Kirkman, M. A.; Bristow, C.; Croal, P.; Plaha, P.; Campo, L.; Chappell, M. A.; Lord, S.; Jenkinson, M. D.; Middleton, M. R.; Sibson, N. R. VCAM-1-targeted MRI Improves Detection of the Tumor-brain Interface. *Clin. Cancer Res.* **2022**, *28* (11), 2385–2396.
- (25) Xu, T.; Ding, W.; Ji, X.; Ao, X.; Liu, Y.; Yu, W.; Wang, J. Molecular mechanisms of ferroptosis and its role in cancer therapy. *J. Cell Mol. Med.* **2019**, *23* (8), 4900–4912.
- (26) Li, J.; Cao, F.; Yin, H. L.; Huang, Z. J.; Lin, Z. T.; Mao, N.; Sun, B.; Wang, G. Ferroptosis: past, present and future. *Cell Death Dis.* **2020**, *11* (2), 88.
- (27) Wang, Y.; Wu, J.; Chen, H.; Yang, Y.; Xiao, C.; Yi, X.; Shi, C.; Zhong, K.; He, H.; Li, Y.; Wu, Z.; Zhou, G.; Rao, Q.; Wang, X.; Zhou, X.; Lomber, G.; Liu, B.; Zhao, J.; Ge, J.; Zhou, W.; Chu, X.; Chen, C.; Zhou, X.; Wang, L.; Guan, K.; Qu, L. Genome-wide CRISPR-Cas9 screen identified KLF11 as a druggable suppressor for sarcoma cancer stem cells. *Sci. Adv.* **2021**, DOI: 10.1126/sciadv.abe3445.
- (28) Moussalli, M. J.; Wu, Y.; Zuo, X.; Yang, X. L.; Wistuba, I. I.; Raso, M. G.; Morris, J. S.; Bowser, J. L.; Minna, J. D.; Lotan, R.; Shureiqi, I. Mechanistic contribution of ubiquitous 15-lipoxygenase-1 expression loss in cancer cells to terminal cell differentiation evasion. *Cancer Prev Res. (Phila)* **2011**, *4* (12), 1961–72.
- (29) Kazan, H. H.; Urfali-Mamatoglu, C.; Yalcin, G. D.; Bulut, O.; Sezer, A.; Banerjee, S.; Gunduz, U. 15-LOX-1 has diverse roles in the resensitization of resistant cancer cell lines to doxorubicin. *J. Cell Physiol* **2020**, *235* (5), 4965–4978.
- (30) Tian, R.; Zuo, X.; Jaoude, J.; Mao, F.; Colby, J.; Shureiqi, I. ALOX15 as a suppressor of inflammation and cancer: Lost in the link. *Prostaglandins Other Lipid Mediat.* **2017**, *132*, 77–83.
- (31) Papenfort, K.; Sun, Y.; Miyakoshi, M.; Vanderpool, C. K.; Vogel, J. Small RNA-mediated activation of sugar phosphatase mRNA regulates glucose homeostasis. *Cell* **2013**, *153* (2), 426–37.
- (32) Sarker, D.; Plummer, R.; Meyer, T.; Sodergren, M. H.; Basu, B.; Chee, C. E.; Huang, K. W.; Palmer, D. H.; Ma, Y. T.; Evans, T. R. J.; Spalding, D. R. C.; Pai, M.; Sharma, R.; Pinato, D. J.; Spicer, J.; Hunter, S.; Kwatra, V.; Nicholls, J. P.; Collin, D.; Nutbrown, R.; Glenny, H.; Fairbairn, S.; Reebye, V.; Voutila, J.; Dorman, S.; Andrikakou, P.; Lloyd, P.; Felstead, S.; Vasara, J.; Habib, R.; Wood, C.; Saetrom, P.; Huber, H. E.; Blakey, D. C.; Rossi, J. J.; Habib, N. MTL-CEBPA, a Small Activating RNA Therapeutic Upregulating C/EBP-alpha, in Patients with Advanced Liver Cancer: A First-in-Human, Multicenter, Open-Label, Phase I Trial. *Clin. Cancer Res.* **2020**, *26* (15), 3936–3946.
- (33) Tan, X.; Jia, F.; Wang, P.; Zhang, K. Nucleic acid-based drug delivery strategies. *J. Controlled Release* **2020**, *323*, 240–252.
- (34) Liu, X.; Guo, Q.; Gao, G.; Cao, Z.; Guan, Z.; Jia, B.; Wang, W.; Zhang, K.; Zhang, W.; Wang, S.; Li, W.; Hao, Q.; Zhang, Y.; Li, M.; Zhang, W.; Gu, J. Exosome-transmitted circCABIN1 promotes Temozolomide resistance in glioblastoma via sustaining ErbB downstream signaling. *J. Nanobiotechnol.* **2023**, *21* (1), 45.